The Astrophysical Journal, 901:94 (8pp), 2020 October 1 https://doi.org/10.3847/1538-4357/abaf5a

Cause and Kinematics of a Jetlike CME

Reetika Joshi[1], Yuming Wang[2,3], Ramesh Chandra[1], Quanhao Zhang[2], Lijuan Liu[4], and Xiaolei Li[2]
[1] Department of Physics, DSB Campus, Kumaun University, Nainital—263 001, India; reetikajoshi.ntl@gmail.com
[2] CAS Key Laboratory of Geospace Environment, School of Earth and Space Sciences, University of Science and Technology of China, Hefei, People's Republic of China
[3] CAS Center for Excellence in Comparative Planetology, University of Science and Technology of China, Hefei 230026, People's Republic of China
[4] School of Atmospheric Sciences, Sun Yat-sen University, Zhuhai, Guangdong, 519000, People's Republic of China
Received 2020 April 22; revised 2020 July 22; accepted 2020 August 12; published 2020 September 25

Abstract

In this article, we present the multiviewpoint and multiwavelength analysis of an atypical solar jet based on data from Solar Dynamics Observatory, SOlar and Heliospheric Observatory, and Solar TErrestrial RElations Observatory. It is generally believed that coronal mass ejections (CMEs) develop from the large-scale solar eruptions in the lower atmosphere. However, the kinematical and spatial evolution of the jet on 2013 April 28 suggests that the jet was clearly associated with a narrow CME with a width of ≈25° and speed of ≈450 km s^{-1}. To better understand the link between the jet and the CME, we performed a coronal potential field extrapolation from the line-of-sight magnetogram of the active region. The extrapolations suggest that the jet eruption follows the same path of the open magnetic field lines from the source region, which provides a route for the jet material to escape from the solar surface toward the outer corona.

Unified Astronomy Thesaurus concepts: Solar magnetic fields (1503); Solar activity (1475); The Sun (1693); Solar coronal mass ejections (310)

Supporting material: animations

1. Introduction

The solar jet is a common phenomenon of small-scale plasma ejections from the solar lower atmosphere toward the solar corona. A solar flare, or the base brightening at the jet footpoint, is believed to promote the force for pushing the plasma material upward. After the first observational evidence of solar jets by Shibata et al. (1992) using Yohkoh satellite observations in X-rays, jets have become a popular research topic in solar physics. They have been studied by many authors (Canfield et al. 1996; Alexander & Fletcher 1999; Filippov et al. 2009; Nisticò et al. 2009; Hong et al. 2011; Schmieder et al. 2013; Liu et al. 2014, 2016, 2019; Sterling et al. 2015; Chandra et al. 2017b; Kayshap et al. 2018; Ruan et al. 2019). From the previous reported results, it is now well accepted that 68% of solar jets are active region (AR) jets (Shimojo et al. 1996; Sterling et al. 2017) and the length, velocity, and width have average values of ≈1 × 10^4–5 × 10^5 km, 100–800 km s^{-1}, and 10^3–10^5 km, respectively (Chandra et al. 2015; Sterling et al. 2016; Joshi et al. 2017). Raouafi et al. (2016) provides a comprehensive review of coronal jet phenomena, including observations, theory, and numerical simulations.

According to the eruption process, Moore et al. (2010) classified solar jets into two subclasses, i.e., standard and blowout jets. In a standard jet, the core field of the base arch remains close and static, whereas in a blowout jet it explodes and results in a breakout eruption. They further clarified that about two-thirds of the observed X-ray jets fall in the standard picture of jets and one-third are in the blowout category. The division of coronal jets into two categories is a result of the shear/twist in the base arch of the jet. Blowout jets usually have a high shear/twist in the base to erupt and open (Liu et al. 2009; Chandra et al. 2017b). Helicity can be transferred from the closed field into the open field due to the reconnection between them. This ejection of helicity causes the upward motion of the jet material by nonlinear torsional Alfvèn waves (Pariat et al. 2009; Liu et al. 2019). The magnetic reconnection between the closed and open field lines is the cause of magnetic flux emergence and cancellation. The continuous magnetic flux cancellation and emergence destabilize the field at the jet base.

Coronal mass ejections (CMEs) interest solar physicists because they play a significant role in affecting the Earth's space environment. Usually, CMEs are associated with large-scale solar eruptions, i.e., two-ribbon flares (Joshi et al. 2016; Zuccarello et al. 2017), filament eruptions (Schmieder et al. 2013; Chandra et al. 2017a), and occasionally with small-scale solar eruptions, i.e., solar jets (Shen et al. 2012; Liu et al. 2015; Zheng et al. 2016; Sterling 2018). Shen et al. (2012) reported two simultaneous CMEs associated with a blowout jet. One of the two CMEs was bubblelike and the other was jetlike. The authors suggested that the external magnetic reconnection produced the jetlike CME and also led to the rise of a small filament underneath the jet base. Further, they explained that the bubblelike CME was due to the internal reconnection of the magnetic field lines. Liu et al. (2015) observed a coronal jet event that led to a high-speed CME (1000 km s^{-1}), suggesting that large-scale eruptions could be triggered by a small-scale jet. Zheng et al. (2016) reported a similar event in a case study of solar jet activity that developed into a CME eruption.

However, the number of such jet–CME cases is too small for us to understand the mechanism and kinematic processes behind the phenomenon. Here, we present a jet event followed by a CME on 2013 April 28 that provides evidence of clear association of the jet and the CME. The jet erupted with an initial speed of ≈200 km s^{-1} and developed into a CME together with the ambient coronal structures. The paper is structured as follows. We present the data analysis in Section 2. The kinematics of the jet and CME is given in Section 3. The magnetic field configuration of the jet source region is

described in Section 4. We discuss and summarize our results in Section 5

2. Data

The observational data for the jet eruption and the CME are taken from the Solar Dynamics Observatory (SDO, Pesnell et al. 2012), Solar TErrestrial RElations Observatory (STEREO, Kaiser et al. 2008), and Large-Angle Spectrometric Coronagraph (LASCO, Brueckner et al. 1995) on board the SOlar and Heliospheric Observatory (SOHO, Domingo et al. 1995). The Atmospheric Imaging Assembly (AIA, Lemen et al. 2012) on board SDO observes the Sun in seven EUV/UV wavelengths with a spatial resolution of 0.″6 and a cadence of 12 s. For the multithermal jet structure, we analyzed the AIA data in 131, 171, 193, 211, and 304 Å. For a better contrast between the hot and cool counterparts of the jet, we created the base and running difference images of the AIA data. To probe the jet and CME from multiple perspectives, the EUV images taken by the Sun Earth Connection Coronal and Heliospheric Investigation (Howard et al. 2008) on board STEREO were analyzed. The twin spacecraft of the STEREO mission, STEREO-A and STEREO-B, observe the Sun from two angles in four different EUVI channels, 171 (Fe IX), 195 (Fe XII), 284 (Fe XV), and in 304 (He II) Å. For our current analysis of the jet, we use the EUV images of STEREO-B in 304 Å with a cadence of 10 minutes and pixel size of 1″. STEREO-A and B were separated by 83° on 2013 April 28. To correct the projection effect of the speed of jet, we use the SCC_MEASURE routine available in the SolarSoft library in IDL. In this routine the "tiepointing" technique is used to reconstruct the three-dimensional picture of the ejecting feature, by clicking the same feature on both STEREO and SDO images (Thompson 2006; Gosain et al. 2009).

The CME is well observed with SOHO/LASCO and STEREO/COR coronagraphs. STEREO COR1 has a field of view from 1.5 to 4 $R_\odot$ and provides images with a cadence of 5 minutes, while COR2 observes the corona from 2 to 15 $R_\odot$. LASCO observed the CME in the outer corona up to 30 $R_\odot$ with a cadence of 12 (C2) and 30 (C3) minutes. With the multipoint observations from LASCO and COR, we employ the Graduated Cylindrical Shell (GCS) model to obtain the three-dimensional height and direction of the CME (see Section 3.2). We further analyze the photospheric magnetic field using the line-of-sight (LOS) magnetograms from the Helioseismic and Magnetic Imager (HMI, Schou et al. 2012) on board SDO. For a closer and clearer view of the jet source region, we use the HMI Spaceweather HMI Active Region Patch (SHARP, Bobra et al. 2014) data set with a cadence of 12 minutes.

3. Kinematics

3.1. Kinematics of the Solar Jet

The jet started to erupt at ≈20:53 UT with a circular base, toward the northern direction from the AR NOAA 11731 (N09E23), and was observed in all six AIA channels (94, 131, 171, 193, 211, and 304 Å). After reaching a height of about 80 Mm, the jet material was deflected from its original direction of propagation and revolved around the northeast direction. The jet was initially bright (Figure 1(a2)), and afterward followed with dark material (Figure 1(a1)), suggesting impulsively strong heating at the initial phase. The subsequent dark material was only visible in AIA 304 Å and not observed in hot channels, i.e., 171 Å. The propagation of the whole jet in AIA 304 Å is shown in Figure 1(a1) along with the red curve C1, which indicates the deflection of the jet from north to northeast toward the solar limb. The initiation of the jet from the source region is shown in panel (a2). We also observed a small jet ejection at about 21:24 UT in the eastern neighborhood of the source region, and this jet material merged with the big jet (see the animation for Figure 1). Panel (b1) is the height–time plot of the jet along slit C1. The jet speed shows a two-stage profile. The speed in the later stage is about 80 km s^{-1} toward the northeast (red dotted line). To find the velocity in the initial stage, we set two slits, S1 and S2 (panel (a2)), of 10 pixel width in two different directions, and found that the speed in the S1 direction is 200 km s^{-1} and that for S2 is about 160 km s^{-1} (as presented in panels (b2) and (b3)). In addition to this, we found that a portion of the jet material falls back to the source region around 21:51 UT with a speed of ≈60 km s^{-1}, which is clear in the height–time plot along the S2 direction in panel (b3).

From ≈21:16 UT, STEREO-B observed the cool counterpart of a jet in 304 Å above the western limb. The full-disk image of AIA 304 Å and STEREO-B EUV 304 Å is presented in Figure 2. The highest visible peak of the jet is indicated with a circle at the solar limb, which is used to determine the real jet speed. Figure 3 (panel (c)) shows the locations of STEREO, the Earth, and the Sun. With the aid of the SCC_Measure procedure, we find the real speed and propagation direction of the jet by clicking on the same feature in AIA 304 Å and in the STEREO-B 304 Å image. The real jet speed was 200 km s^{-1} toward the northeast (longitude = −18°, latitude = 19°) direction. However, this correction could be only applied to the second stage of the jet when it was propagating northeast, because we do not have stereoscopic observations for the early stage of the jet.

3.2. Kinematics of the CME

The associated CME was well observed with SOHO/LASCO and STEREO-B COR1 and COR2 coronagraphs, as shown in Figure 3. The CME is atypical. It is narrow (width ≈ 25°), and resembles a giant jet in the corona, no matter which perspective is used to view the CME. The jet-CME association is very much evident in STEREO-B observations (see Figure 3(e) and the attached animation). For the continuous tracking of the solar jet in the EUV channel (304 Å) and the CME in coronagraphs, we put a slit in the jet-CME direction in STEREO-B EUV 304 Å, COR1, and COR2. The direction of the slit is shown in Figure 3(a). The continuous spatial and temporal correlation between the jet and the CME is presented in Figure 3(e). The front of the CME is much higher than the jet front and the separation between them is due to the expansion of the CME, causing the speeds of their fronts to be different. If extrapolated back to the solar surface, they almost originated at the same time.

To reduce the projection effect, we use the GCS model to determine the real kinematic properties of the CME. The GCS model is developed to represent the flux rope structure of CMEs (Thernisien et al. 2006; Thernisien 2011). It involves three geometric parameters: "h," the height of the leading edge, "κ," the aspect ratio, and "δ," the half edge-on angular width, and three positioning parameters: "θ," "ϕ," and "γ," the Stonyhurst latitude and longitude of the source region, and the tilt angle of the source region neutral line, respectively. The

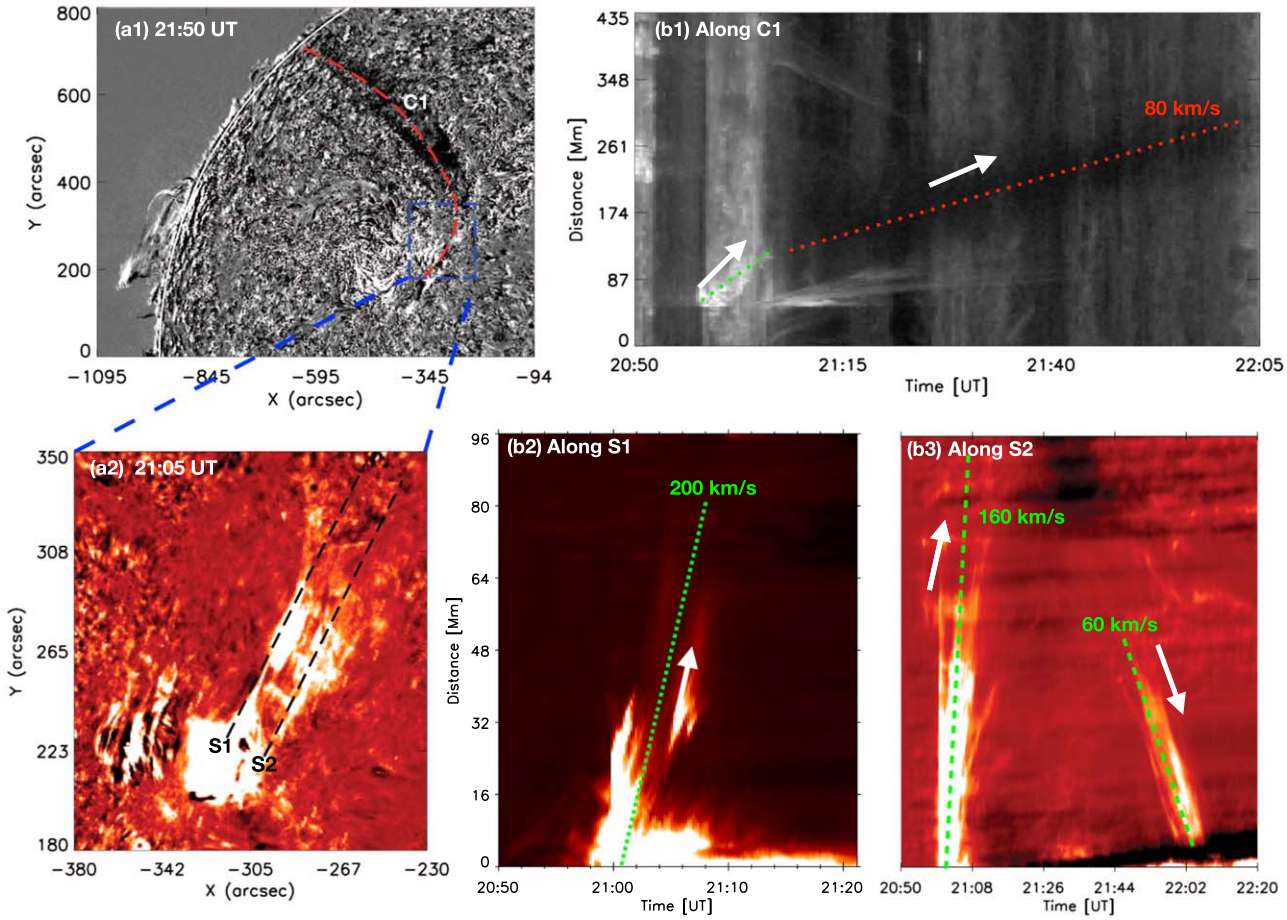

Figure 1. Observed jet (a1)–(a2) and height–time analysis (b1)–(b3) with AIA 304 Å on 2013 April 28 from NOAA AR 11731. Panel (a1) shows the direction of jet propagation from the source region (blue rectangular box) toward the solar limb as a red dashed curve and (b1) is the spacetime plot along curve C1. The jet starts with a speed of ≈200 km s^{-1}. Panel (a2) is the location of the jet source region, which is indicated by the blue rectangular box in panel (a1). Panels (b2) and (b3) are the height–time analysis along slits S1 and S2, respectively, indicated in panel (a2). In the direction of slit S2, the jet material falls back into the source region with a speed of ≈60 km s^{-1}. The animation of panels (a1) and (b2) presents the jet eruption from its base toward the eastern limb from 20:50 UT to 21:57 UT.

(An animation of this figure is available.)

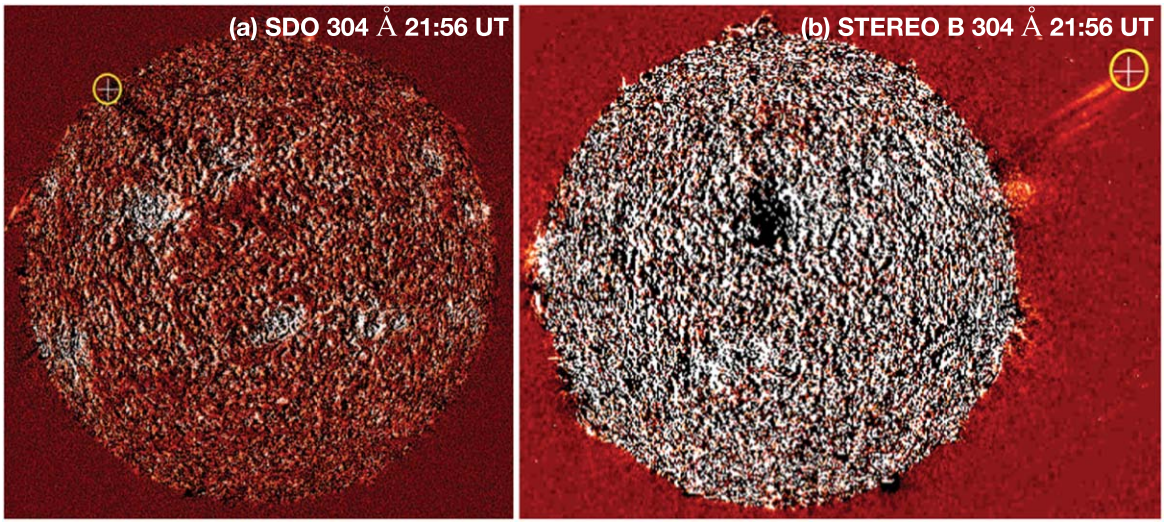

Figure 2. Leading edge of the jet material in SDO/AIA 304 Å (a) and in STEREO-B EUV 304 Å (b). The + sign encircled with a yellow circle shows the location of the leading edge of the jet at 21:56 UT. These two positions of the leading edge of jet are obtained from the SCC_MEASURE technique that is used for the jet velocity calculation.

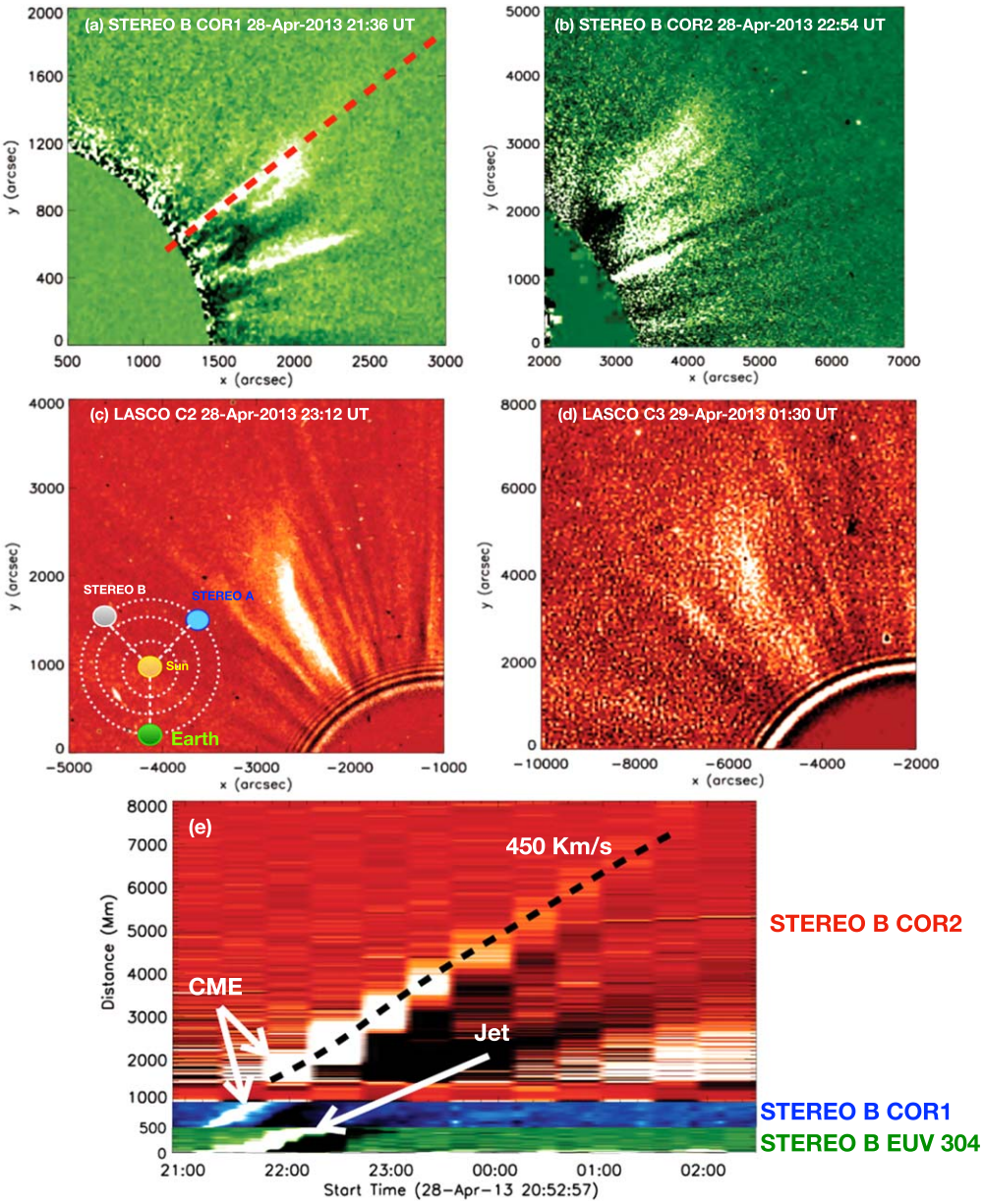

Figure 3. CME associated with the jet is observed by LASCO and STEREO coronagraphs. Top: the observed CME in STEREO-B COR1 and COR2. Middle: the observed CME in LASCO C2 and the C3 field of view. The locations of STEREO-A, STEREO-B, and the Earth on 2013 April 28 are shown in panel (c). Bottom: height–time analysis of the jet and jetlike CME observed with STEREO-B EUVI 304 Å (green), COR1 (blue), and COR2 (red). The direction of the slit for this height–time analysis is shown in panel (a) with red dashed line. The separation between the CME front and jet front is due to the expansion of the jetlike CME. They almost originated from the same location when extrapolated back to the solar surface. The animation for the jet-CME association with STEREO-B shows the jet eruption observed with STEREO-B EUV 304 Å from 2013 April 28 20:36 UT to 2013 April 29 00:06 UT, STEREO-B COR1 from 2013 April 28 21:00 to 22:10 UT, and STEREO-B COR2 from 2013 April 28 20:54 UT to 2013 April 29 03:24 UT.

(An animation of this figure is available.)

GCS model is usually used to study the morphology, position, and kinematics of a CME based on the best-fitting result of a CME transient recorded in white-light images. The ice cream cone model is another model for CMEs, and is comprised of a ball that we call the ice cream ball and a circular cone tangent to the ball with a conic node on the solar surface (Fisher & Munro 1984). The GCS model becomes equivalent to the ice cream cone model when its parameter δ equals 0 (Thernisien 2011). For our case study, we used a ice cream cone model that is a simplified form of the GCS model and estimated the three-dimensional height and direction of the CME with LASCO C2, C3, and STEREO-B COR2 images. The best-fitted GCS model is displayed in Figure 4. The corrected CME speed from the GCS model comes out to be 450 km s^{-1}.

Figure 5(a) depicts the complete kinematics of the jet and the CME with the different data points of various instruments. We have corrected the projection effect for the jet and CME with SCC_MEASURE and GCS model fitting, respectively. For SCC_MEASURE, the corrected jet speed comes out to be $\approx$200 km s^{-1} for a CME with a speed $\approx$450 km s^{-1}. The blue and red represent corrected and uncorrected data points. This plot of temporal evolution shows the clear link between the jet and the narrow CME. Figure 5(b) shows the intensity variation at the jet base. The impulsive peaks at the jet base show the jet

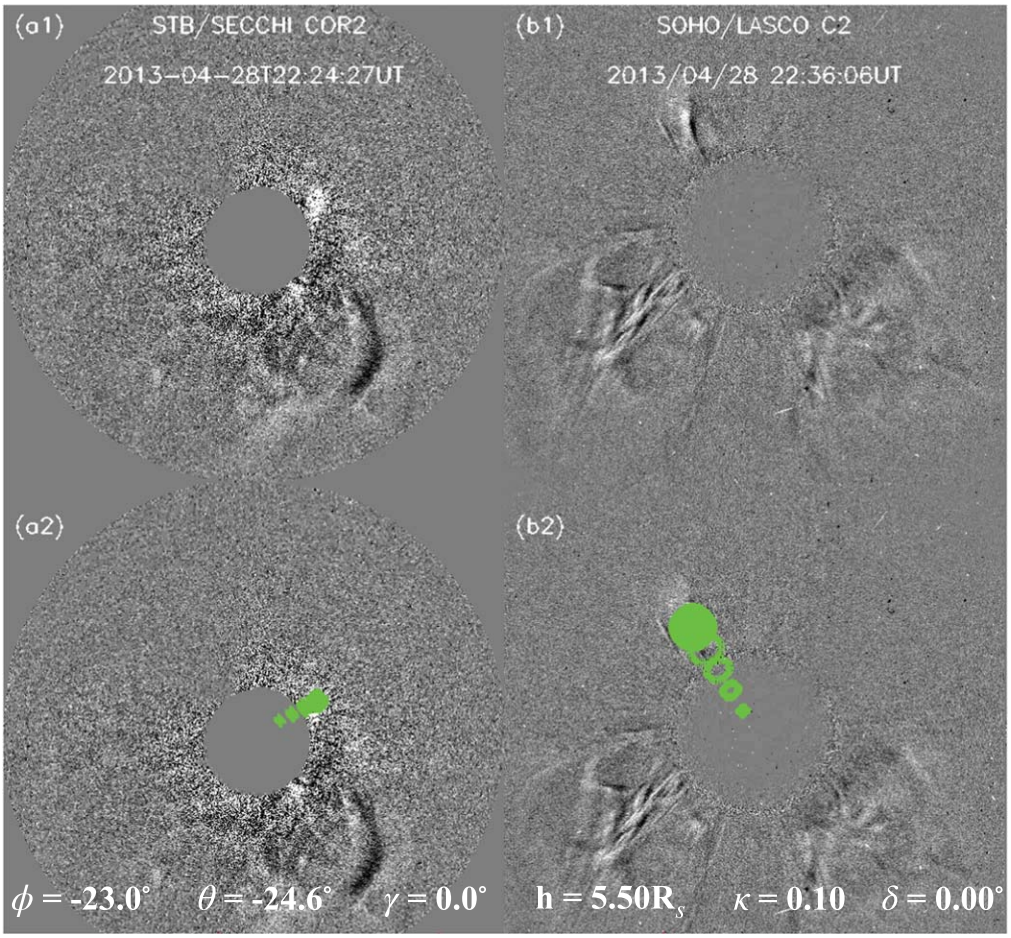

Figure 4. CME associated with the jet eruption is analyzed with the GCS model, which indicates the direction of propagation of the CME in STEREO-B, COR2, and LASCO C2, with a speed of ≈450 km s^{-1}.

peak time in various AIA wave bands. The enhancement in the light curve of EUV emission suggests that energy injection occurred only at the very beginning, and is not responsible for the continuous acceleration of the jet to escape from the Sun.

The speed of the CME (450 km s^{-1}) is much larger than that of a jet (200 km s^{-1}). This is because the speeds of different parts of erupting structures are measured. The speed of the CME obtained from the STEREO and LASCO observations is at its leading edge ($v_{\rm front}$). It consists of the propagation speed of the CME center ($v_{\rm center}$) and the expansion speed ($v_{\rm exp}$) of the CME, so $v_{\rm front} = v_{\rm center} + v_{\rm exp}$. A cartoon illustrating the CME speed at the leading edge, and including the CME propagation speed and expansion speed, is featured in Wang et al. (2015; see their Figure 1). Gopalswamy et al. (2009) derived a relation between CME propagation speed and expansion that has been confirmed in many studies until now (Michalek et al. 2009; Mäkelä et al. 2016). With an approximation of the CME shape by a shallow ice cream cone, the relationship is defined as $v_{\rm exp} = 2\ v_{\rm front}\ \sin(w/2)$, where "$w$" is the CME width (25° in present case). Therefore, $v_{\rm exp}$ comes out to be 230 km s^{-1} and $v_{\rm center}$ should be 220 km s^{-1}. The jet triggered and developed into the CME and its trajectory should be followed by the CME center and not by the leading edge of the CME. Thus, the jet velocity (200 km s^{-1}) is comparable with $v_{\rm center}$ ($v_{\rm center} < v_{\rm front}$). That explains the difference between the jet and CME speeds.

4. Magnetic Configuration of the Source Region

For a better understanding of the trigger mechanism of the solar jet, we did the magnetic field analysis of the source region using the HMI SHARP data (12 minute cadence) of AR 11731 on 2013 April 28. The continuous cancellation of the negative magnetic polarity by the emerging positive magnetic spot is observed (Figure 6 and accompanying animation). The positive magnetic polarity ate the negative magnetic polarity that was already distributed in the jet source region (plotted inside the green circle in panels (a) and (g)). Afterward, small negative polarities emerged from the large negative ball and were canceled by the large positive polarity area. The emergence of small negative polarities is shown with yellow arrows and the cancellation is indicated with cyan arrows. To look at the variation of the magnetic flux with time, we calculated the positive, negative, and total unsigned magnetic flux at the jet source region, which is indicated as the red rectangular box in panel (e). This is the same dimensional area we used to calculate the light curve in Figure 5(b). The flux variation with time in panel (j) shows that there is a continuous cancellation and emergence of negative magnetic flux (blue line), while a positive magnetic flux emerges throughout (red curve). The total unsigned magnetic flux (black curve) shows the simultaneous cancellation and emergence of magnetic polarities at the jet source region. The emergence of the positive magnetic flux dominated over the cancellation throughout. The initiation of jet time is shown with a green dashed vertical line.

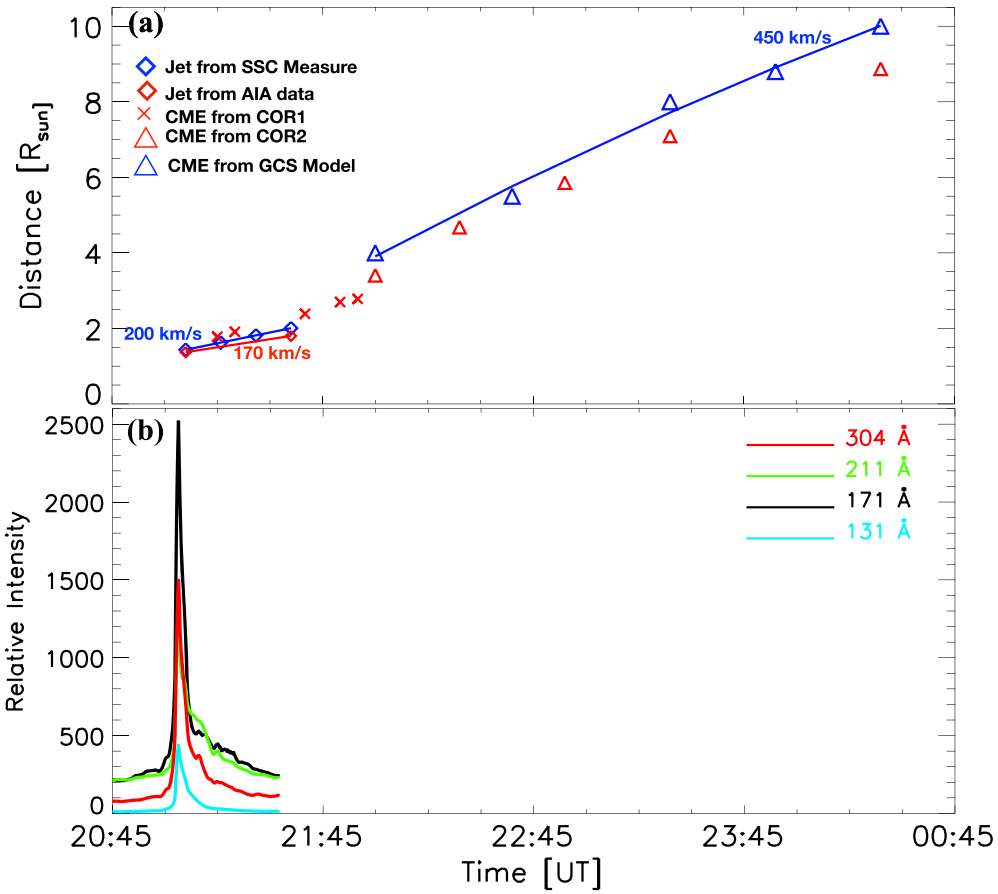

Figure 5. Panel (a): the complete kinematics of the jet and the CME. The projection-corrected speeds are plotted in blue, while the red points are used for uncorrected data. Panel (b): light curves for different wavelengths. These are observed at the jet base shown as the red rectangular box presented in Figure 6(e).

We analyzed the magnetic topology at the jet location and applied two different methods of potential extrapolation, one for the global overview of the jet eruption, and the other for the local view at the jet base region. The details are as follows:

We apply the Potential Field Source Surface (PFSS) model (Schrijver & De Rosa 2003) to investigate the global magnetic topology near the jet source region. This PFSS technique uses the HMI synoptic magnetic maps processed with a software package available in SSWIDL. We apply the PFSS technique to see the reconnection between close loops and open field lines, because at large scales the corona is in a potential state (Schmieder et al. 1996). The PFSS model for this case study is presented in Figure 7(a), with open (pink) and closed (white) magnetic field lines. These open field lines resemble the path the jet follows, moving north in the beginning and deflecting northeast afterward.

To describe the magnetic topology of the jet base region, we extrapolate the coronal potential field using the photospheric LOS magnetogram as a boundary condition. Our method is based on the Fourier transformation (FT) method proposed by Alissandrakis (1981). The FT method requires the vertical component of the photospheric vector field to be the input parameter. However, due to the HMI vector magnetic field's limited FOV, the extrapolation does not easily meet the divergence-free condition. Hence, we cut a larger patch of the LOS magnetogram instead. As the AR is close to the central meridian, the LOS magnetic field could represent the vertical field to a large extent. In the extrapolated magnetic field, we find that open field lines coincide well with the extension direction of the jet shown in Figures 7(b) and (c).

5. Discussion and Summary

In this article, we investigate a solar jet eruption from the AR NOAA 11731 on 2013 April 28. The jet was ejected north, and after reaching a height of 80 Mm was deflected northeast. The average computed speed of the jet was ≈200 km s^{-1}. We found a clear association of the observed jet with a narrow CME of speed 450 km s^{-1}, observed in LASCO C2, C3, and STEREO-B COR1, and the COR2 coronagraph.

The escape speed of the Sun is given as $v = \sqrt{\frac{2GM_{\odot}}{R}}$, where R is the distance from the center of the Sun. The observed jet speed computed using the multiviewpoint observations is about 200 km s^{-1} at a height of 2 $R_{\odot}$. The escape velocity computed at the height of 2 $R_{\odot}$ using the above formula is ≈430 km s^{-1}. Therefore, we conclude that the complete jet could not have escaped from the solar surface. This could why we have observed the backward motion of the jet material from the propagation direction toward the source region. Even though jet speed is lower than the escape speed, we observed a clear CME associated with the jet in all the spaceborne coronagraphs. The possible mechanism for the jet continuously accelerating to reach the escape speed and form the narrow CME is material falling back and making the upward material of the jet move faster to conserve the momentum of the whole jet. We concluded that the observed speed of the CME contains

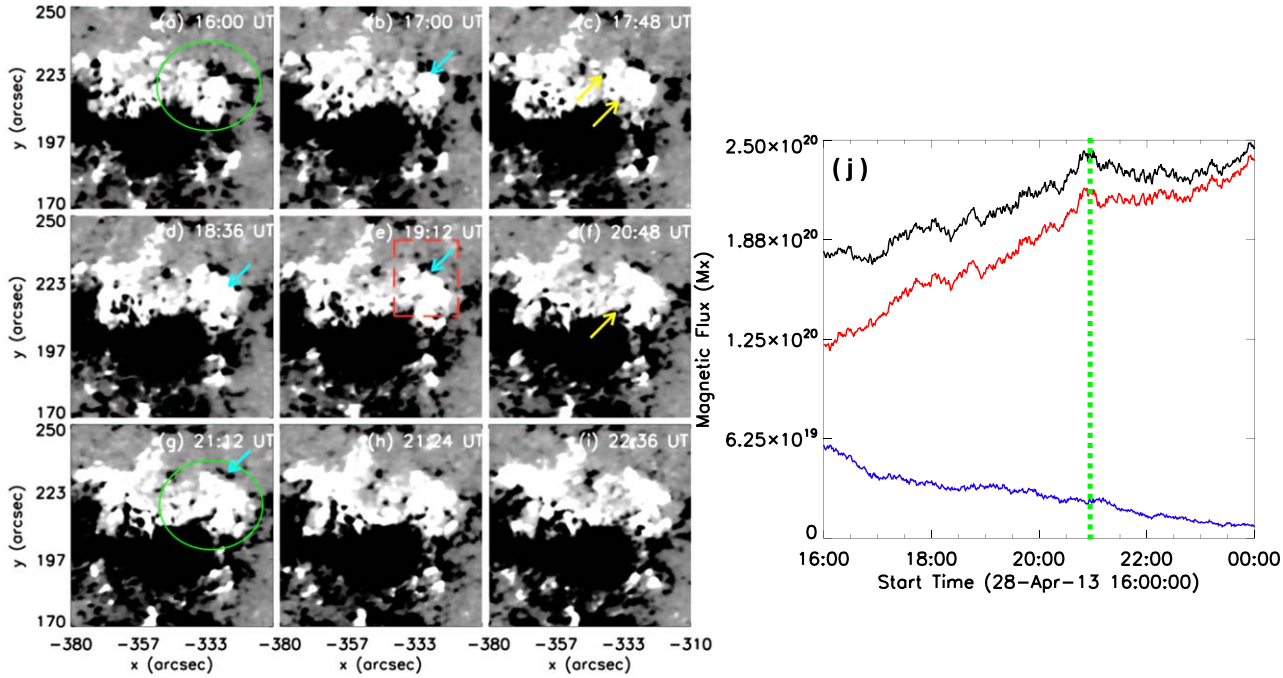

Figure 6. Left panels (a)–(i) show the magnetic field configuration at the jet site. The cyan and yellow arrows show the cancellation and emergence of negative magnetic polarity. The emergence of positive magnetic polarity is enclosed by the green circle in panels (a) and (g). The right panel (j) is the magnetic flux variation, with time calculated at the jet source region indicated as a red rectangular box in the left panel (e). Jet starting time is highlighted with a green dashed line. The black, red, and blue curves are for the total, positive, and negative magnetic flux, respectively. The animation shows the magnetic field evolution (a)–(i) from 16:00 UT to 22:36 UT.

(An animation of this figure is available.)

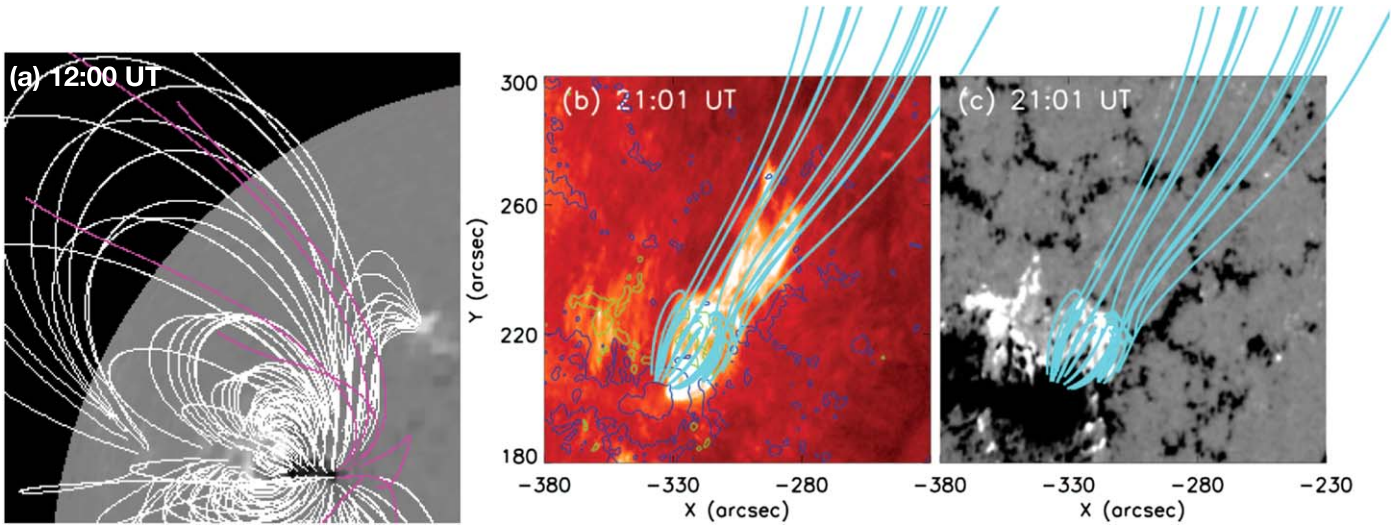

Figure 7. PFSS extrapolation of the large field of view (FOV) is shown in panel (a). The white and pink lines are the closed and open magnetic field lines at the jet location. The open field lines mirror the jet propagation from its source to the solar corona, which is indicated as curve C1 in Figure 1(a1). Panels (b) (AIA 304 Å) and (c) (HMI magnetogram) show the jet source region with the same FOV as the blue rectangular box in Figure 1(a1). The cyan lines from the source region are the magnetic field lines, which shows a closed structure at the jet base and open lines afterward. The blue and green contours in panel (b) represent negative and positive magnetic fields.

the speed of the CME center and the expansion speed, and is much larger than the jet speed, because different parts of the erupting structures are being measured. The speed of the CME center (the trajectory followed by the jet) is 220 km s^{-1} and is equivalent to the speed of the jet (200 km s^{-1}). This provides clear evidence of the jet–CME association.

For the magnetic configuration at the jet origin site, two views are popular. The first understanding is that the magnetic configuration is the magnetic flux emergence observed in many observations and also proposed in the MHD simulations (Shibata et al. 1992; Yokoyama & Shibata 1995, 1996; Moreno-Insertis et al. 2008; Moreno-Insertis & Galsgaard 2013; Ruan et al. 2019; Joshi et al. 2020). The other view is that the configuration is magnetic flux cancellation, which is also reported in the observations and MHD simulations (Pariat et al. 2009; Young & Muglach 2014; Chandra et al. 2017b; McGlasson et al. 2019). We have also studied the magnetic field evolution in our investigation and observed that there is a

continuous emergence and cancellation of the negative magnetic flux and positive flux emerges throughout. Therefore, we believe that both the flux emergence and the cancellation are responsible in our case.

In the potential field extrapolation, we have found that the jet source region is covered (or overlaid) by the closed field lines and open field lines. The open field lines are in the direction of the jet ejection. We have attempted the nonlinear force-free field (NLFFF) extrapolation, but it failed to reproduce the magnetic field topology of the AR. The field lines of the NLFFF did not resemble the loops observed in the EUV passbands. This might have happened because the FOV of the photospheric vector magnetic field provided by HMI SHARP data is too small, as it is available for a significant AR patch of the solar magnetic field. Hence, the divergence-free condition is not completely satisfied in the extrapolation, which makes the NLFFF results unreliable. On the other hand, we mainly focus on the propagation of the jet, which is more likely relevant to the nearly potential, large-scale magnetic field connectivity. Therefore, we believe that the potential field extrapolation might be sufficient and the direction of the jet ejection is the same as that of the open magnetic field lines we have obtained from the potential field extrapolation (see Figure 7). Hence, we conclude that the reconnection between the closed and open magnetic field lines provides a path for the ejection of the jet.

We also observed the rotation in the jet material when it is propagating north from the source region (see the animation of Figure 1). The untwisting of the jet suggests an injection of helicity into the upper atmosphere.

In summary, our study of a narrow CME caused by a jet gives evidence that some jets from the solar disk can escape from the corona to form a CME, which may contribute to space weather phenomena. In a future study, we look forward to finding clear in situ measurements for such jetlike CMEs from the newly launched Parker Solar Probe.

We thank the anonymous referee for valuable comments that significantly improved our manuscript. We thank the SDO, STEREO, and SOHO science teams for the free access to the data. R.J. thanks the SCOSTEP Visiting Scholarship program for providing the opportunity to carry this work at the University of Science and Technology China (USTC) and the Department of Science and Technology (DST), New Delhi India, for the INSPIRE fellowship. R.J. also thanks Dr. Arun K. Awasthi for the useful discussion during her visit at USTC. This work is supported by grants from NSFC (No. 41774178 and 41761134088). R.C. acknowledges support from the Bulgarian Science Fund under the Indo-Bulgarian bilateral project. We thank Dr. Brigitte Schmieder for helpful discussions.

ORCID iDs

Reetika Joshi https://orcid.org/0000-0003-0020-5754
Yuming Wang https://orcid.org/0000-0002-8887-3919
Ramesh Chandra https://orcid.org/0000-0002-3518-5856
Quanhao Zhang https://orcid.org/0000-0003-0565-3206
Lijuan Liu https://orcid.org/0000-0001-6804-848X

References

Alexander, D., & Fletcher, L. 1999, SoPh, 190, 167
Alissandrakis, C. E. 1981, A&A, 100, 197
Bobra, M. G., Sun, X., Hoeksema, J. T., et al. 2014, SoPh, 289, 3549
Brueckner, G. E., Howard, R. A., Koomen, M. J., et al. 1995, SoPh, 162, 357
Canfield, R. C., Reardon, K. P., Leka, K. D., et al. 1996, ApJ, 464, 1016
Chandra, R., Filippov, B., Joshi, R., & Schmieder, B. 2017a, SoPh, 292, 81
Chandra, R., Gupta, G. R., Mulay, S., & Tripathi, D. 2015, MNRAS, 446, 3741
Chandra, R., Mandrini, C. H., Schmieder, B., et al. 2017b, A&A, 598, A41
Domingo, V., Fleck, B., & Poland, A. I. 1995, SoPh, 162, 1
Filippov, B., Golub, L., & Koutchmy, S. 2009, SoPh, 254, 259
Fisher, R. R., & Munro, R. H. 1984, ApJ, 280, 428
Gopalswamy, N., Dal Lago, A., Yashiro, S., & Akiyama, S. 2009, CEAB, 33, 115
Gosain, S., Schmieder, B., Venkatakrishnan, P., Chandra, R., & Artzner, G. 2009, SoPh, 259, 13
Hong, J., Jiang, Y., Zheng, R., et al. 2011, ApJL, 738, L20
Howard, R. A., Moses, J. D., Vourlidas, A., et al. 2008, SSRv, 136, 67
Joshi, N. C., Schmieder, B., Magara, T., Guo, Y., & Aulanier, G. 2016, ApJ, 820, 126
Joshi, R., Chandra, R., Schmieder, B., et al. 2020, A&A, 639, A22
Joshi, R., Schmieder, B., Chandra, R., et al. 2017, SoPh, 292, 152
Kaiser, M. L., Kucera, T. A., Davila, J. M., et al. 2008, SSRv, 136, 5
Kayshap, P., Murawski, K., Srivastava, A. K., & Dwivedi, B. N. 2018, A&A, 616, A99
Lemen, J. R., Title, A. M., Akin, D. J., et al. 2012, SoPh, 275, 17
Liu, J., Wang, Y., & Erdélyi, R. 2019, FrASS, 6, 44
Liu, J., Wang, Y., Erdélyi, R., et al. 2016, ApJ, 833, 150
Liu, J., Wang, Y., Liu, R., et al. 2014, ApJ, 782, 94
Liu, J., Wang, Y., Shen, C., et al. 2015, ApJ, 813, 115
Liu, W., Berger, T. E., Title, A. M., & Tarbell, T. D. 2009, ApJL, 707, L37
Mäkelä, P., Gopalswamy, N., & Yashiro, S. 2016, SpWea, 14, 368
McGlasson, R. A., Panesar, N. K., Sterling, A. C., & Moore, R. L. 2019, ApJ, 882, 16
Michalek, G., Gopalswamy, N., & Yashiro, S. 2009, SoPh, 260, 401
Moore, R. L., Cirtain, J. W., Sterling, A. C., & Falconer, D. A. 2010, ApJ, 720, 757
Moreno-Insertis, F., & Galsgaard, K. 2013, ApJ, 771, 20
Moreno-Insertis, F., Galsgaard, K., & Ugarte-Urra, I. 2008, ApJL, 673, L211
Nisticò, G., Bothmer, V., Patsourakos, S., & Zimbardo, G. 2009, SoPh, 259, 87
Pariat, E., Antiochos, S. K., & DeVore, C. R. 2009, ApJ, 691, 61
Pesnell, W. D., Thompson, B. J., & Chamberlin, P. C. 2012, SoPh, 275, 3
Raouafi, N. E., Patsourakos, S., Pariat, E., et al. 2016, SSRv, 201, 1
Ruan, G., Jejčič, S., Schmieder, B., et al. 2019, ApJ, 886, 134
Schmieder, B., Demoulin, P., Aulanier, G., & Golub, L. 1996, ApJ, 467, 881
Schmieder, B., Guo, Y., Moreno-Insertis, F., et al. 2013, A&A, 559, A1
Schou, J., Scherrer, P. H., Bush, R. I., et al. 2012, SoPh, 275, 229
Schrijver, C. J., & De Rosa, M. L. 2003, SoPh, 212, 165
Shen, Y., Liu, Y., Su, J., & Deng, Y. 2012, ApJ, 745, 164
Shibata, K., Ishido, Y., Acton, L. W., et al. 1992, PASJ, 44, L173
Shimojo, M., Hashimoto, S., Shibata, K., et al. 1996, PASJ, 48, 123
Sterling, A. C. 2018, JPhCS, 1100, 012024
Sterling, A. C., Moore, R. L., Falconer, D. A., & Adams, M. 2015, Natur, 523, 437
Sterling, A. C., Moore, R. L., Falconer, D. A., Panesar, N. K., & Martinez, F. 2017, ApJ, 844, 28
Sterling, A. C., Moore, R. L., Falconer, D. A., et al. 2016, ApJ, 821, 100
Thernisien, A. 2011, ApJS, 194, 33
Thernisien, A. F. R., Howard, R. A., & Vourlidas, A. 2006, ApJ, 652, 763
Thompson, W. T. 2006, A&A, 449, 791
Wang, Y., Zhou, Z., Shen, C., Liu, R., & Wang, S. 2015, JGRA, 120, 1543
Yokoyama, T., & Shibata, K. 1995, Natur, 375, 42
Yokoyama, T., & Shibata, K. 1996, ApL&C, 34, 133
Young, P. R., & Muglach, K. 2014, SoPh, 289, 3313
Zheng, R., Chen, Y., Du, G., & Li, C. 2016, ApJL, 819, L18
Zuccarello, F. P., Chandra, R., Schmieder, B., Aulanier, G., & Joshi, R. 2017, A&A, 601, A26